PHYSICAL REVIEW E **75**, 051905 (2007)

Monte Carlo simulations of flexible polyelectrolytes inside viral capsids with dodecahedral charge distribution

Daniel George Angelescu[*] and Per Linse
Physical Chemistry 1, Lund University, Box 124, SE-221 00 Lund, Sweden

(Received 18 December 2006; published 9 May 2007)

Structural properties of encapsidated flexible polyelectrolytes in viral capsids with dodecahedral charge distribution have been investigated by Monte Carlo simulations using a coarse-grained model. Several capsid charge distributions ranging from a homogeneous surface charge distribution ($\lambda = 0$) to a complete dodecahedral distribution ($\lambda = 1$) at constant total capsid charge and fixed radial location of the capsid charges have been considered. The radial and lateral organizations of the polyelectrolyte have been examined as a function of the polyelectrolyte length and capsid charge distribution. With short polyelectrolytes a single polyelectrolyte layer was formed at the inner capsid surface, whereas at increasing polyelectrolyte length also a uniform polyelectrolyte density inside the surface layer was established. At low λ, the polyelectrolyte layer was laterally isotropic, but at $\lambda \geq 0.05$ a dodecahedral structure started to appear. At $\lambda = 1$, the polyelectrolyte followed essentially a path along the edges of a dodecahedron. With sufficiently long chains, all edges were decorated with polyelectrolyte, facilitated by loop formation. For an undercharged capsid, the capsid counterions inside the capsid also adopted a dodecahedral distribution.

DOI: 10.1103/PhysRevE.75.051905 PACS number(s): 87.15.Aa, 82.70.−y

I. INTRODUCTION

A virus particle consists of a shell (capsid) composed of several proteins and a genome inside the capsid. The capsid is often either cylindrical or spherical-like with an icosahedral shape, whereas the genome may consist of DNA or RNA. The flexibility of the genome plays a crucial role of the genome packing inside the capsid. Double-stranded (*ds*)DNA possesses a persistence length of ≈50 nm which is large in comparison to the capsid size. On the other hand, single-stranded (*ss*)DNA and *ss*RNA have a persistence length in the nanometer range which is smaller than the capsid size. In bacteriophages containing *ds*DNA, the genome is tightly packed [1] and a coaxial spool-like structure not reflecting the capsid symmetry has been extensively reported [2–4]. In contrast, encapsidated *ss*RNA may partially adopt the symmetry of the surrounding protein capsid due to its larger flexibility and the much lower genome volume fraction. From geometrical considerations, the genome volume fraction of such ssRNA-containing viruses is estimated to be at most 5% [1,5–8].

Sections of genomic RNA that are symmetrically localized within virus capsids have been visualized by x-ray and neutron crystallography for several $T = 1$ and 3 viruses such as satellite tobacco necrosis virus [9], satellite tobacco mosaic virus [10,11], turnip yellow mosaic virus [12], flock house virus [13], black beetle virus [14], and bluetongue virus [15]. Image reconstruction of noncrystalline MS2 bacteriophage [16] and pariacoto virus [8] (both $T = 3$ viruses) showed that a part of the genome displayed a structure that reflects its electrostatic interaction with the capsid charges.

Regarding the MS2 bacteriophage, 10%–20% of the RNA genome was estimated to take the shape of an icosahedral network around the three- and five-fold axes of the MS2 capsid, whereas the remaining genome was homogeneously distributed. The network was composed of tubular features with a diameter of ≈20 Å, most likely being *ds*RNA. Almost all of the RNA genome in MS2 appears in double stranded structures [16]. In the pariacoto virus, the amount of ordered RNA is ≈35%. Images reconstructed from crystallography and cryoelectron microscopy showed that the genome close to the inner capsid surface was mainly organized as duplex RNA and passes along the edge formed at the junction of twofold symmetry-related asymmetric units [8]. Besides the helical segments at the twofold axes, three of these RNA segments form a three-way junction at the threefold axis of the I_h symmetry group and lead to a dodecahedral structure. The remaining part of the viral RNA inside the capsid surface layer is disordered.

The different pattern of the electrostatic potential generated by the capsid charges at the inner capsid surface (icosahedral for the MS2 phage and dodecahedral for the pariacoto virus) and the similarly different structure of the ordered RNA strongly indicate that the gross structure of the genome is controlled by the electrostatic interaction rather than by the shape of the inner capsid surface. Nevertheless, even in the latter case, the capsid with an icosahedral shape and the ordered RNA with a dodecahedral structure have the same I_h symmetry.

On the basis of x-ray diffraction, it was assumed that RNA-protein interactions are essentially base independent and the genome conformation is driven by the nonspecific electrostatic interactions with the oppositely charged protein shell [17]. Primarily arginine and lysine located in the protein subunits interact with the phosphate group of the genomic RNA, and for a genome with a large degree of order N-terminal extended subunits are found to be inserted in the major groove of the RNA duplex [8]. Furthermore, isopoten-

---

[*] Permanent address: Romanian Academy, Institute of Physical Chemistry "I. G. Murgulescu", Splaiul Independentei 202, 060021 Bucharest, Romania.

tial surfaces of the inner surface of the cowpea chlorotic mottle virus (CCMV) capsid, where the genome is also partially symmetrically localized within the virus [18], calculated in the frame of the Poisson-Boltzmann theory and on the basis of crystallographic data, presented a series of connected bumps at the top of the hexameric and pentameric units, reflecting the symmetry of the virus capsid [19].

Due to electrostatic interactions between the genome and capsid proteins, RNA packaging and capsid formation appear to be intimately connected, even though there are reported cases in which the capsid can be formed in the absence of RNA [20]. RNA would act as a growth template, as in the case of cylindrical viruses [21], but the growth scenario for icosahedral capsid is not well-understood. It is believed that the assembly begins with specific RNA-protein interactions and the subsequent capsid growth is driven by the nonspecific electrostatic interaction. However, unlike the cylindrical viruses, the formation of a dodecahedral structure is facilitated by the existence of a branched secondary structure of *ss*RNA. The reason is that graph topological constraint excludes a linear genome to adopt a dodecahedral structure unless sharp bends are allowed [6]. Consequently, the backbone of RNA molecules covers a Hamiltonian cycle along a subset of the dodecahedron edges, while the side-branches are responsible for covering the rest of the edges. This implies that the size of the secondary structure of the genome will determine the capsid size. Indeed, for viruses with a large amount of RNA genome possessing a dodecahedral structure, such as MS2 bacteriophage and pariacoto, the contour length of the secondary structure of the nonencapsidated genome is comparable with the length of the dodecahedron contour formed by the twofold axes of the icosahedrally shaped capsid.

Since the early atomistic simulation of hydrated *ds*DNA by Celmenti *et al.* [22], short oligonucleotides in aqueous solution have been simulated [23–28]. More long-range properties have been examined by using coarse-grained models, where the *ds*DNA is represented as a wormlike or a spring-bead chain. In particular, the complexation between *ds*DNA and oppositely charged macromolecules, as occurring in the chromatin complex, has been in focus [29–32]. These studies have provided valuable generic properties of isolated and complexed *ds*DNA. This comes not as a complete surprise, since coarse-grained dielectric models have during the last two decades shown to be extremely useful to describe electrolyte solutions as well as solutions of charged macromolecules [33–35].

In our previous work [36], results of Monte Carlo simulations of polyelectrolytes of different flexibilities and lengths confined inside a viral capsid were presented. A coarse-grained model was used, where the genome was represented by a spring-bead chain, the capsid by a spherical shell, and the aqueous solution by a dielectric medium. We investigated the polyelectrolyte conformation and the thermodynamics of the encapsidation process. We found a transition from an isotropic chain distribution at low bare persistence length to a spoollike structure when the bare persistence length was larger than the size of the confining space. Our predicted radial distribution of the genome was later qualitatively reproduced by a full atomistic simulation of the satellite tobacco mosaic virus [37].

The aim of the present study is to obtain further understanding of the conformation of flexible polyelectrolytes inside viral capsids. Here, we extend our previous investigation by considering viral capsids possessing charge distributions with I_h symmetry as found for some $T=3$ viruses. Systematic changes of the capsid charge distribution at constant radial location and total amount of capsid charge were performed to provide a comprehensive picture of the lateral organization of the encapsidated polyelectrolyte. Hence, of concern is the role of the electrostatic interactions for the structure of the encapsidated genome. The simplicity of the model used makes it possible to rationalize the observed features in terms of the different interactions appearing in the systems.

II. MODEL AND METHODS

A. Model system

A coarse-grained model of a scale-reduced $T=3$ virus was used, as in our previous work [36]. The viral capsid is modeled as a spherical shell with an inner radius $R_c=50$ Å and a thickness $D_c=12$ Å. The capsid has a fixed total charge $Z_c^{\text{tot}}=260$ distributed at a radial distance $\Delta=2$ Å from its inner surface. Different distributions of the total capsid charge are considered. The two *extreme* ones are (I) a homogeneous surface charge density and (II) a "dodecahedral" charge distribution. In the latter case, charges are positioned at the vertices and at eight evenly distributed positions along each edge of a dodecahedron projected on a spherical surface with the radius $R_c+\Delta$, resulting in 260 sites each carrying the charge $Z_c=1$ [Fig. 1(a)]. Although the locations of the charges do not generate a true dodecahedron, we will for simplicity still refer it to as a dodecahedron. In particular, the structure still has I_h symmetry. The distance between two adjacent sites becomes 4.19 Å and the total dodecahedral contour length becomes 1131 Å. The fraction λ of the total capsid charge Z_c^{tot} was placed according to distribution II and the remaining fraction $1-\lambda$ according to distribution I, giving a homogeneous surface charge density $\sigma=(1-\lambda)Z_c^{\text{tot}}e/[4\pi(R_c+\Delta)^2]$. Thus a charge distribution parameter $\lambda=0$ corresponds to a homogeneous surface charge density, which generates a constant electrostatic potential inside the capsid, and $\lambda=1$ to the case where the total capsid charge is dodecahedrally distributed.

Figure 1(b) shows the variation of the electrostatic potential for $\lambda=1$ at $r=48$ Å, the distance at which the polyelectrolyte is in contact with the inner capsid surface. The largest electrostatic potential difference occurs between a vertex and a pentagon center and is 6 kT/e. The corresponding map of the electrostatic potential inside a pariacoto virus generated by the capsid charges is displayed in Fig. 1(c). Indeed, our model very closely represents the dodecahedral nature of the electrostatic potential at the inner capsid surface of the pariacoto virus. Nevertheless, there are some details that differ; one is that the largest electrostatic potential appears at the midpoint of a pentagon edge instead of at a vertex. For the

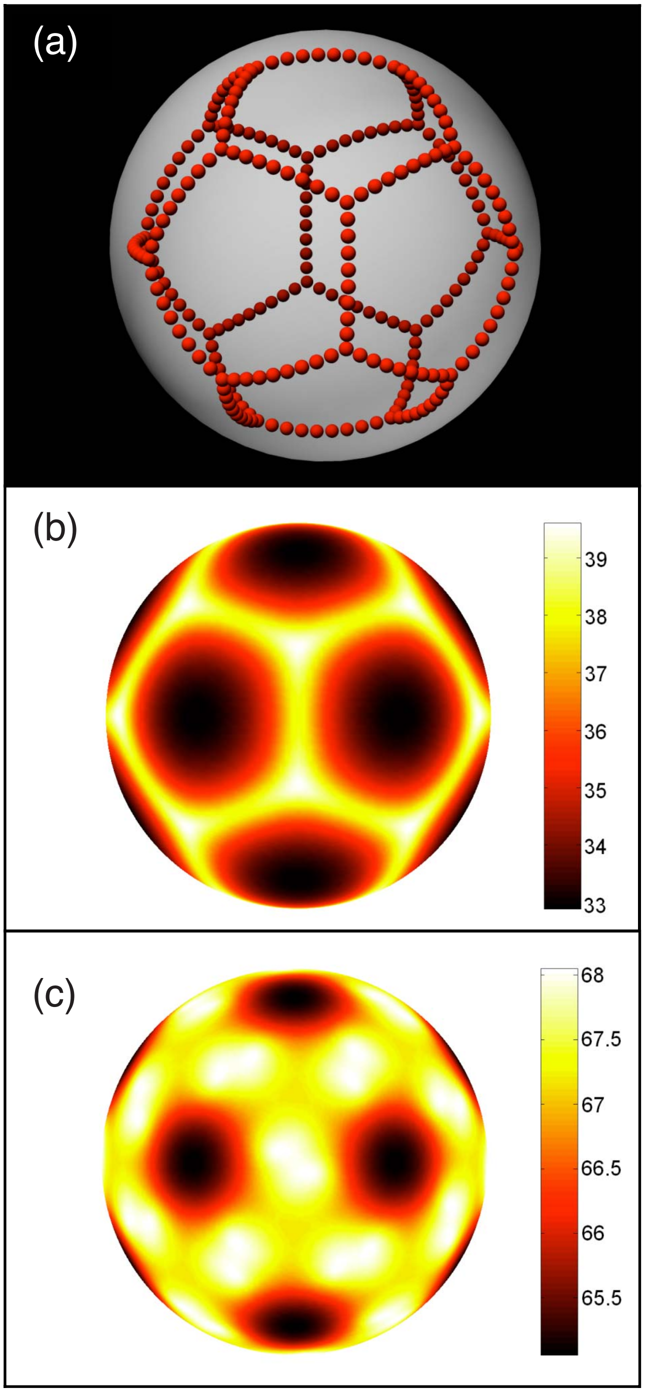

FIG. 1. (Color online) (a) Illustration of the outer capsid surface (gray sphere) of radius $r = R_c + D_c = 62$ Å and the location of 260 charged sites (red spheres), of which 20 are located at the vertices of a dodecahedron and 240 distributed evenly along the projections of the dodecahedron edges on a spherical surface of radius $r = 52$ Å. (b) Electrostatic potential (kT/e units) at the radial distance $r = R_c - R_b = 48$ Å generated by the discrete capsid charge distribution at the charge distribution parameter $\lambda = 1$. (c) Electrostatic potential (kT/e units) at the radial distance $r = 90$ Å generated by the capsid charges of the pariacoto virus; the protein data bank (PDB) identification number is 1F8V and the coordinates of the crystal structure were obtained from Virus Particle Explorer (VIPER) [45].

pariacoto virus, the difference between the extreme values of the electrostatic potential is 2.5 kT/e, which would correspond to $\lambda \approx 0.4$ in our model system.

The polyelectrolyte is described as a linear chain of N_b monovalently negatively charged hard spheres (beads). The beads are joined by a harmonic bond potential and the intrinsic chain stiffness is regulated by a harmonic angular potential. In addition, monovalently charged capsid and polyelectrolyte counterions, separately neutralizing the charge of the two macroions, are present. The small ions are modeled as charged hard spheres, each bearing one unit charge. The aqueous solution and the capsid are treated as dielectric continua with the same relative permittivity.

The four different types of particles, viz. (i) the positively charged capsid; (ii) the negatively charged beads of the polyelectrolyte; (iii) the capsid counterions; and (iv) the polyelectrolyte counterions, are all confined in a spherical cell with the radius R_{cell}. The purpose of the cell is to make the model represent a system at finite capsid concentration. The precise value of R_{cell} is of less importance [36]. Finally, the polyelectrolyte beads are confined inside the capsid, whereas the small ions are free to cross the capsid.

In more detail, the total potential energy U can be divided into four terms according to

$$U = U_{\text{nonbond}} + U_{\text{bond}} + U_{\text{angle}} + U_{\text{cell}}. \tag{1}$$

The nonbonding term U_{nonbond} is the sum of two contributions,

$$U_{\text{nonbond}} = \sum_{i<j} u_{ij}(r_{ij}) + \sum_{i} u_{\text{c},i}(r_i), \tag{2}$$

of which the first one represents the hard-sphere and Coulomb interactions between charged particles according to

$$u_{ij}(r_{ij}) = \begin{cases} \infty, & r_{ij} < R_i + R_j \\ \dfrac{Z_i Z_j e^2}{4\pi\varepsilon_0\varepsilon_r r_{ij}}, & r_{ij} \geq R_i + R_j, \end{cases} \tag{3}$$

where i and j denote either a polyelectrolyte bead or a small ion, r_{ij} the distance between centers of particles i and j, R_i the hard-sphere radius of particle i, Z_i the valence of particle i, ε_0 the dielectric permittivity of vacuum, and ε_r the relative permittivity of the system. The second term of Eq. (2) represents the interaction between mobile particles and the capsid and is given by

$$u_{\mathrm{c},i}(r_i)=\begin{cases}\infty, & R_\mathrm{c}-R_i<r_i<R_\mathrm{c}+D_\mathrm{c}+R_i\\ (1-\lambda)\dfrac{Z_\mathrm{c}^{\mathrm{tot}}Z_ie^2}{4\pi\varepsilon_0\varepsilon_\mathrm{r}(R_\mathrm{c}+\Delta)}+\lambda\displaystyle\sum_{j=1}^{260}\dfrac{Z_iZ_je^2}{4\pi\varepsilon_0\varepsilon_\mathrm{r}|\mathbf{r}_i-\mathbf{r}_j|}, & r_i<R_\mathrm{c}-R_i\\ (1-\lambda)\dfrac{Z_\mathrm{c}^{\mathrm{tot}}Z_ie^2}{4\pi\varepsilon_0\varepsilon_\mathrm{r}|\mathbf{r}_i|}+\lambda\displaystyle\sum_{j=1}^{260}\dfrac{Z_iZ_je^2}{4\pi\varepsilon_0\varepsilon_\mathrm{r}|\mathbf{r}_i-\mathbf{r}_j|}, & r_i>R_\mathrm{c}+D_\mathrm{c}+R_i,\end{cases}\tag{4}$$

where $\mathbf{r}_i$ denotes the position of particle i (polyelectrolyte bead or small ion) and $\mathbf{r}_j$ the position of capsid charge j. The two finite terms represent the interaction between particle i with the homogeneous and discrete capsid charge distribution, respectively.

The bond energy U_bond, entering as the second term of Eq. (1), is given by

$$U_\mathrm{bond}=\sum_{i=1}^{N_\mathrm{b}-1}\frac{k_\mathrm{bond}}{2}(r_{i,i+1}-r_0)^2,\tag{5}$$

where N_b is the number of polyelectrolyte beads, $r_{i,i+1}$ the distance between two bonded beads, r_0 the equilibrium bond distance (r_0=5 Å), and k_bond the bond force constant (k_bond =0.4 N m^{-1}). The root-mean-square (rms) bead-bead separation becomes $\langle R_\mathrm{bb}^2\rangle^{1/2}$=5.5–5.9 Å for the different systems investigated.

The bond-bond angular potential energy U_angle of Eq. (1) is represented by

$$U_\mathrm{angle}=\sum_{i=2}^{N_\mathrm{b}-1}\frac{k_\mathrm{angle}}{2}(\alpha_i-\alpha_0)^2,\tag{6}$$

where α_i is the angle between the vectors $\mathbf{r}_{i+1}-\mathbf{r}_i$ and $\mathbf{r}_{i-1}-\mathbf{r}_i$ made by three consecutive beads, α_0 the equilibrium angle ($\alpha_0=180°$), and k_angle the angular force constant. Here, $k_\mathrm{angle}=0.51\times10^{-24}$ J deg^{-2} has been used, corresponding to the bare persistence length l_p^0=8.5 Å, as evaluated for an uncharged polymer according to the relation $l_\mathrm{p}^0=\langle R_\mathrm{bb}^2\rangle^{1/2}/(1+\langle\cos\alpha\rangle)$ [38]. This bare persistence length is suitable to describe homopolymeric *ss*RNA. The ratio of the persistence length and the inner capsid radius becomes $l_\mathrm{p}^0/R_\mathrm{c}\approx0.2$, implying that bending energy arising from the encapsidation of the polyelectrolyte is small.

Finally, the last term U_cell entering in Eq. (1) describes the confining cell potential. It is given by

$$U_\mathrm{cell}=\sum_i u_\mathrm{cell}(r_i),\tag{7}$$

where

$$u_\mathrm{cell}(r_i)=\begin{cases}\infty, & r_i>R_\mathrm{cell}\\ 0, & r_i\le R_\mathrm{cell}\end{cases}\tag{8}$$

and affects only the small ions.

B. Systems

Systems comprising different (i) polyelectrolyte length and (ii) capsid charge distribution have been considered. The number of polyelectrolyte beads selected are N_b=100, 183, 260, 400, and 600. Hence the ratio of the polyelectrolyte charge and the total capsid charge defined by $\beta\equiv|N_\mathrm{b}Z_\mathrm{b}/Z_\mathrm{c}^{\mathrm{tot}}|$ ranges from $\beta<1$ (undercharged capsid) to $\beta>1$ (overcharged capsid) and includes $\beta=1$ (charge-neutral polyelectrolyte-capsid complex). For the longest chain (N_b =600), the ratio of the contour length of the polyelectrolyte and the interior circumference of the capsid becomes $(N_\mathrm{b}-1)\langle R_\mathrm{bb}^2\rangle^{1/2}/(2\pi R_\mathrm{c})\approx11$. The largest volume fraction of polyelectrolyte beads inside the capsid is 4%. As mentioned earlier, the charge distribution parameter λ brings continuously a homogeneous surface charge distribution (λ=0) to a dodecahedral distribution (λ=1).

Throughout, T=298 K and ε_r=78.4 have been used. Values of the parameters characterizing the model and data of the T=3 phage are summarized in Table I. Obviously, the model is only a coarse-grained representation of a T=3 phage. In particular, we do not include any structural details on a molecular level, including capsid symmetry or secondary structure of *ss*RNA. We also neglect the variation of the relative dielectric permittivity and the effect of 0.1M salt present under physiological conditions, the latter attenuating the electrostatic interaction.

C. Simulation details

Structural equilibrium properties of the model system were obtained by performing Metropolis Monte Carlo (MC) simulations in the canonical ensemble. All interactions within the cell were considered, and hence no potential cutoff was applied.

In the Metropolis sampling, the polyelectrolyte was subjected to three kinds of trial displacements: (i) single-bead move; (ii) pivot rotation of a randomly selected part of the polyelectrolyte; and (iii) slithering move. The probability of a pivot rotation was 1/100 and of a slithering move 1/10 to 1/100 times the probability of the single-bead move. Small ions were subjected to single-particle displacements only.

Initial configurations were generated by placing the polyelectrolyte randomly inside the capsid and the small ions randomly inside the cell, subjected to hard-sphere and capsid overlap tests. After equilibration involving 5×10^4 passes (attempted moves per particle), the production runs comprised typically 5×10^5 passes. The reported uncertainties

TABLE I. General data of the model and the main characteristics of the $T=3$ virus.

Variable	Symbol	Model	$T=3$ virus
	Capsid		
Capsid inner radius	R_c	50 Å	100 Å
Capsid thickness	D_c	12 Å	25 Å
Total capsid charge	Z_c^{tot}	260	≈2000–2300
Charge distribution parameter	λ	0 to 1	
Capsid charge	Z_c	+1	+1
Anion charge	Z_-	−1	−1
Anion radius	R_-	2 Å	
	Polyelectrolyte		
Number of polyelectrolyte beads	N_{b}	100–600	≈4500
Bead charge	Z_{b}	−1	−1
Bead radius	R_{b}	2 Å	
Bead separation	$\langle R_{\text{bb}}^2\rangle^{1/2}$	5 to 6 Å	5.6 Å
Bare persistence length	l_{p}^0	8.5 Å	
Cation charge	Z_+	+1	+1
Cation radius	R_+	2 Å	
	Simulation cell		
Radius of sphere[a]	R_{cell}	500–668 Å	

[a] Adjusted to a counterion number density $\rho_- + \rho_+ = 6.87 \times 10^{-7}$ Å^{-3}.

were calculated by dividing the total simulation in ten subbatches and are presented as one standard deviation of the mean. All simulations were performed using the integrated Monte Carlo-molecular dynamics-Brownian dynamics simulation package MOLSIM [39].

D. Structural characterization

Because of the electrostatic interactions in the system, the polyelectrolyte is preferentially located close to the inner capsid surface [36]. Different lateral polyelectrolyte structures may be envisioned, depending on the capsid charge distribution as described by λ. In addition to a disordered lateral structure appearing at λ=0 [36], a dodecahedral structure, reflecting the capsid charge distribution, is anticipated at not too small λ.

The appearance of I_{h} symmetry and a dodecahedral structure of the encapsidated polyelectrolyte was analyzed by using rotational-invariant bond-order parameters introduced by Steinhardt *et al.* [40]. They defined a "bond" as the vector joining a central atom to one of its neighbors. In the present study, the position vector of bead i, $\mathbf{r}_i$, with respect to the center of the cell will represent a bond. For the moment we disregard the radial component of $\mathbf{r}_i$ and define

$$Q_{lm}(\mathbf{r}_i) \equiv Y_{lm}[\theta(\mathbf{r}_i), \varphi(\mathbf{r}_i)], \tag{9}$$

where $Y_{lm}(\theta,\varphi)$ are the spherical harmonics [41] and $\theta(\mathbf{r}_i)$ and $\varphi(\mathbf{r}_i)$ are the polar and azimuthal angle of $\mathbf{r}_i$. Next, we average over all the beads according to

$$\bar{Q}_{lm} = \frac{1}{N_b}\sum_{i=1}^{N_b} Q_{lm}(\mathbf{r}_i), \tag{10}$$

and form the two rotational invariants

$$Q_l = \left(\frac{4\pi}{2l+1}\sum_{m=-l}^{l} |\langle \bar{Q}_{lm}\rangle|^2\right)^{1/2}, \tag{11}$$

$$W_l = \sum_{m_1,m_2} \begin{pmatrix} l & l & l \\ m_1 & m_2 & -m_1-m_2 \end{pmatrix} \langle \bar{Q}_{lm_1}\rangle \langle \bar{Q}_{lm_2}\rangle \times \langle \bar{Q}_{l-(m_1+m_2)}\rangle, \tag{12}$$

where ⟨ ⟩ denotes an ensemble average and the term in brackets in Eq. (12) a Wigner 3j-symbol [41]. Eventually, the parameter S_l involving ratios Q_l and W_l is defined according to

$$S_l = \left(\frac{4\pi}{2l+1}\right)^{3/2} \frac{W_l}{Q_l^3}. \tag{13}$$

In the following, we will use only $l=6$ for symmetry reasons because Q_6 and W_6 are the lowest nonzero invariants for structures possessing I_{h} symmetry [40]. The quantities Q_6 and W_6 can be used to assess how well particles attain the structure formed by the edges of a dodecahedron, and they will be referred to as order parameters. Unlike Q_6 and W_6, $|S_6| = S_6^{I_{\text{h}}}$ with $S_6^{I_{\text{h}}} = 0.169\,754$ *independently* of the degree of lateral heterogeneity *provided* that I_{h} symmetry is present. For spherical symmetry, $S_6=0$. Hence S_6 constitutes a convenient quantity to assess the presence of I_{h} symmetry of the encapsidated polyelectrolyte. Therefore we will refer to S_6 as a symmetry parameter. More specifically, for the distribution shown in Fig. 1(a), we have $Q_6^{\text{dodec}} = 0.281\,96$, $W_6^{\text{dodec}} = 0.004\,004$, and $S_6^{\text{dodec}} = S_6^{I_{\text{h}}}$. We also note that for an icosahedral distribution $S_6^{\text{ico}} = -S_6^{I_{\text{h}}}$.

For the longer chains, the exploration of all symmetry related configurations was slow as compared to the simulation length. Such an exploration is not a necessary requirement for obtaining equilibrium results, but necessary to quantify the dodecahedral structure using the quantity $\bar{Q}_{lm}$. This was remedied by including a symmetrization by averaging of $\bar{Q}_{lm}$ over the 12 five fold axes of the dodecahedron [see Fig. 1(a)].

III. RESULTS

We will first consider the radial distribution of encapsidated polyelectrolytes at different polyelectrolyte length and capsid charge distribution. It will be followed by a discussion on the lateral polyelectrolyte distribution, and, in particular, on its dodecahedral structure. Thereafter some aspects of the distribution of the small ions will be given.

A. Radial polyelectrolyte distribution

Figure 2 shows the bead number density $\rho_{\text{b}}(r)$ as a function of the radial distance for polyelectrolyte-containing

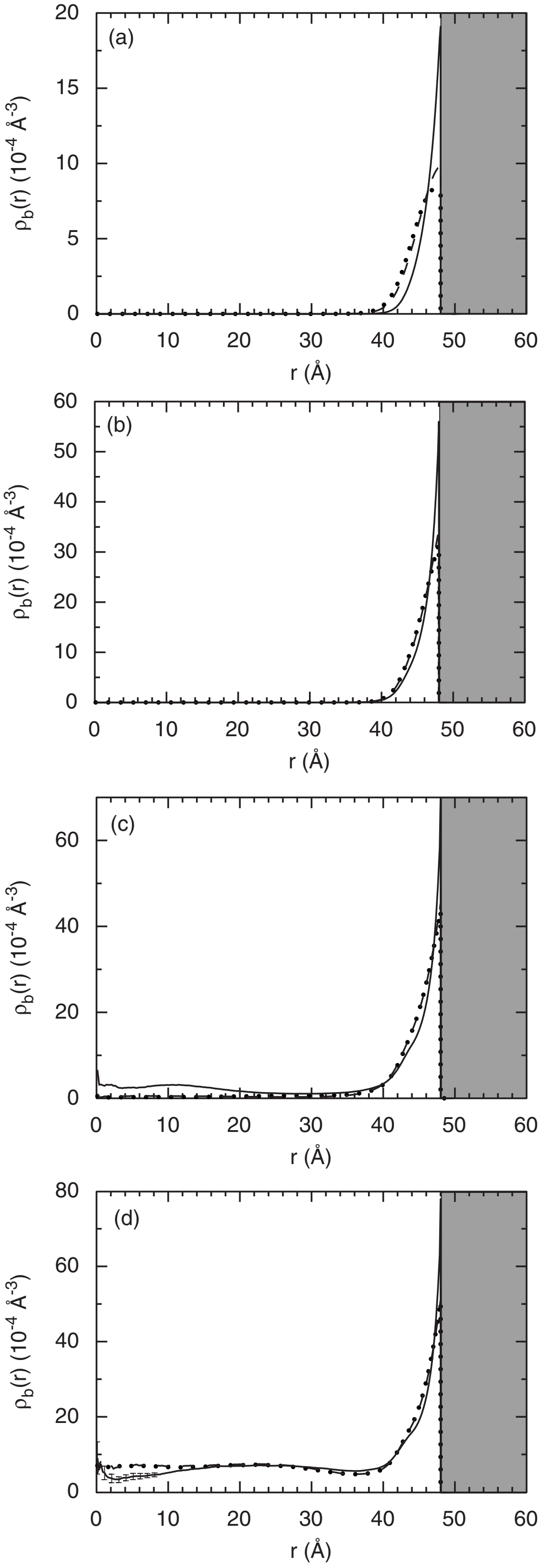

FIG. 2. Bead number density $\rho_b(r)$ as a function of radial distance r for encapsidated polyelectrolyte with (a) $N_b=100$, (b) 260, (c) 400, and (d) 600 beads at charge distribution parameter $\lambda=0.1$ (dotted curves), 0.3 (dashed curve), and 1 (solid curves). The shaded area shows the capsid.

capsids at a different number of beads N_b and different values of the charge distribution parameter λ. It is seen that the radial bead distributions are more influenced by the polyelectrolyte length than the capsid charge distribution.

First, with $N_b=100$ and 260, corresponding to the charge ratios $\beta=0.38$ and 1, respectively, the polyelectrolyte is completely adsorbed at the inner capsid surface in a layer 5–8 Å thick. The extension of the layer is the same with $N_b=100$ and 260 beads, only the number density varies. With $N_b=400$ and 600, corresponding to $\beta=1.54$ and 2.31, still an adsorbed layer at the inner capsid appears, now comprising ≈ 370 beads. The peculiar feature that the charge of the adsorbed polyelectrolyte layer overcompensates the capsid charge can be understood in terms of the electrostatic bead-bead repulsion that is responsible for the polyelectrolyte accumulation at the capsid inner surface. The remaining beads are to a first approximation distributed uniformly inside the surface layer, with the bead density in this inner region increasing with increasing N_b. In the following, will refer to the two regions as (i) the surface layer (40 Å$<r\leq 48$ Å) and (ii) the inner region ($r\leq 40$ Å), respectively, of the interior volume of the capsid.

Now we turn to the influence of the capsid charge distribution on the radial bead density. First, in the limit of $\lambda=0$ (data not shown), the radial distribution $\rho_b(r)$ is practically indistinguishable from that at $\lambda=0.1$. Hence despite the constant electrostatic potential inside the capsid arising from the homogeneous surface charge density distribution ($\lambda=0$), the polyelectrolyte displays a very strong adsorption onto the inner capsid surface. This adsorption originates (i) from the repulsive interactions among the polyelectrolyte beads and (ii) indirectly from the capsid charges through their counterions. A strong adsorption of the polyelectrolyte beads to the inner capsid surface enables the release of the capsid counterions from the neighborhood of the capsid surfaces [36]. Independently of N_b, Fig. 2 shows that (i) the surface layer of beads becomes narrower and (ii) the bead density at the inner capsid surface is higher at increasing λ. Hence introducing spatial heterogeneities of the capsid charge distribution strengthens the polyelectrolyte adsorption onto the inner capsid surface. This is an expected trend; any rearrangement of the charges from a homogeneous distribution (under the conservation of the average electrostatic potential) should lead to an increased adsorption. The important result is that this effect is small.

B. Lateral polyelectrolyte distribution

The angular distribution of the polyelectrolyte beads inside the capsid is referred to as their lateral distribution. Throughout, averages were made over the 12 pentagons [see Fig. 1(a)] by rotating the coordinates of the beads located in the pentagonal pyramids formed by a pentagon and the center of the capsid to a single pentagonal pyramid. Further symmetrization by using the fivefold symmetry axis of the pentagon was not made. The analyses of the lateral distribution were made for beads located in the surface layer and in the inner region separately.

1. Surface layer

We will start by considering the bead angular density σ_b obtained by taking into account beads located in the surface

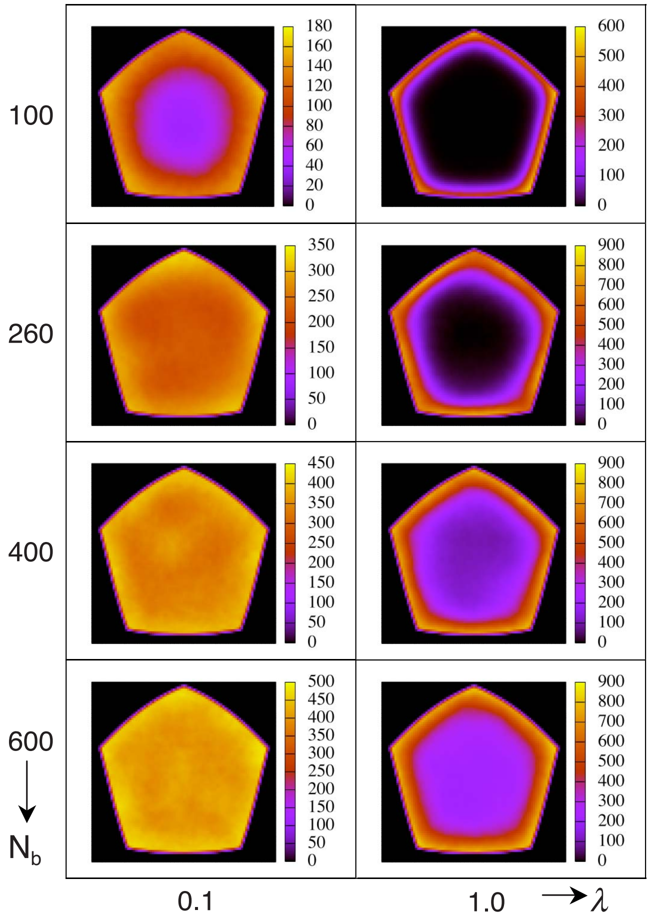

FIG. 3. (Color online) Contour plot of bead angular density σ_b over one pentagon of the dodecahedron at $N_b = 100$, 260, 400, and 600 beads (top to bottom) and charge distribution parameter $\lambda = 0.1$ and 1 (left to right) for beads in the surface layer ($40\ \text{Å} < r \leq 48\ \text{Å}$). Color code: high density (yellow), intermediate density (red), and zero density (black). The unit of σ_b is sr^{-1} and the integral $\int\int \sigma_b(\theta,\varphi)\sin\theta d\theta d\varphi$ over the unit sphere is 4π times the number of beads in the surface layer.

layer. We have normalized σ_b such that the integral of σ_b over the unit sphere gives 4π times the number of beads in the surface layer. Figure 3 displays such contour plots over a pentagon for different values of N_b and λ.

We see that with only 10% of the total capsid charge distributed in a dodecahedral structure ($\lambda = 0.1$), the lateral ordering of the polyelectrolyte beads is substantial for the shortest polyelectrolyte ($N_b = 100$), noticeable for $N_b = 260$, but apparently small for the two longest polyelectrolytes. When the total capsid charge is distributed according to a dodecahedron ($\lambda = 1$), the lateral ordering of the beads becomes very strong. Not unexpectedly, the highest bead densities occur along the vertices of the pentagon and a depletion region appears inside the pentagon. In the case of the strongest lateral segregation appearing at $N_b = 100$ and $\lambda = 1$, almost the entire interior of the pentagon is polyelectrolyte free; hence the polyelectrolyte is strongly confined to the edges of the pentagon. Throughout, the contour plots display a nearly perfect fivefold symmetry, supporting sufficient simulation length.

The lateral ordering of the polyelectrolyte beads will now be considered in more detail by quantifying the bead angular density σ_b along the arclength from a vertex to the midpoint of the opposite edge of a pentagon. Figure 4 shows σ_b as a function of $\cos\theta$, where $\cos\theta = -0.61$ corresponds to a vertex and $\cos\theta = 0.52$ to the midpoint of the opposite edge, at different N_b and λ for beads in the surface layer. Panels (c) and (d) also contain data for the inner region, which will be discussed later. Our main observations are as follows.

(1) Beads are relocated from the inner region of the pentagon toward vertices and edges at increasing λ. Hence as the spatial variation of the electrostatic potential attaining dodecahedral structure becomes more accentuated, the spatial distribution of the polyelectrolyte beads also displays a dodecahedral pattern.

(2) At increasing chain length, a larger charge distribution parameter is needed to achieve similar relocation. For example, at $\lambda = 0.1$ with $N_b = 100$ the bead distribution becomes weakly perturbed from a uniform density, whereas with $N_b \geq 100$ the bead distribution remains basically uniform (as also concluded from Fig. 3).

(3) Typically, the bead density is larger at a vertex than at a midpoint. This behavior is related to the fact that the electrostatic potential generated by the capsid charges is higher at the vertices than along the pentagon edges [see Fig. 1(b)]. However, $N_b = 260$ constitutes an exception.

(4) At increasing N_b, the magnitude of σ_b increases but its increase is only marginal after $N_b = 400$. Hence the number of beads positioned along the pentagon contour increases with the total number of beads until the surface layer is saturated [see also Fig. 2, panels (c) and (d)].

To get further insight into the lateral chain organization, the order parameters Q_6 and W_6 defined by Eqs. (11) and (12) and the symmetry parameter S_6 given by Eq. (13) were calculated for various chain lengths and charge distribution parameters. In the following, only data for Q_6 and S_6 will be given, since W_6 provides essentially the same information as Q_6 but in a more compressed scale. Figure 5 provides the normalized quantities Q_6/Q_6^{dodec} and S_6/S_6^{dodec} as a function of λ for different values of N_b, where Q_6^{dodec} and S_6^{dodec} denote the values for Q_6 and W_6 for the spatial distribution given in Fig. 1(a). If we restrict to a transition between spherical and I_h symmetry, we have the boundaries $0 \leq Q_6/Q_6^{\text{dodec}} \leq a$ and $|S_6/S_6^{\text{dodec}}| \leq 1$ for the normalized quantities with $a \approx 1$. The value of a depends slightly on the number of sites along the dodecahedral edge. For example, the relative difference is 0.3% for six (typical for the polyelectrolyte) and eight (capsid charge distribution) sites.

The order parameter Q_6 given in Fig. 5(a) shows that the beads in the surface layer adhere progressively to the dodecahedral edges of the discrete capsid charge distribution as the charge distribution parameter λ is increased. This is consistent with the lateral ordering exhibited in Fig. 3, implying that Q_6 can be used as a single parameter to represent the degree of lateral ordering. In particular, Q_6/Q_6^{dodec} increases markedly after $\lambda \approx 0.05$ as the fraction of beads positioned along the dodecahedron edges becomes important. At low ($N_b \leq 183$) and at large ($N_b \geq 400$) numbers of beads, the Q_6/Q_6^{dodec} versus λ curves are relatively insensitive of the value of N_b. The value of Q_6/Q_6^{dodec} at large λ reduces sig-

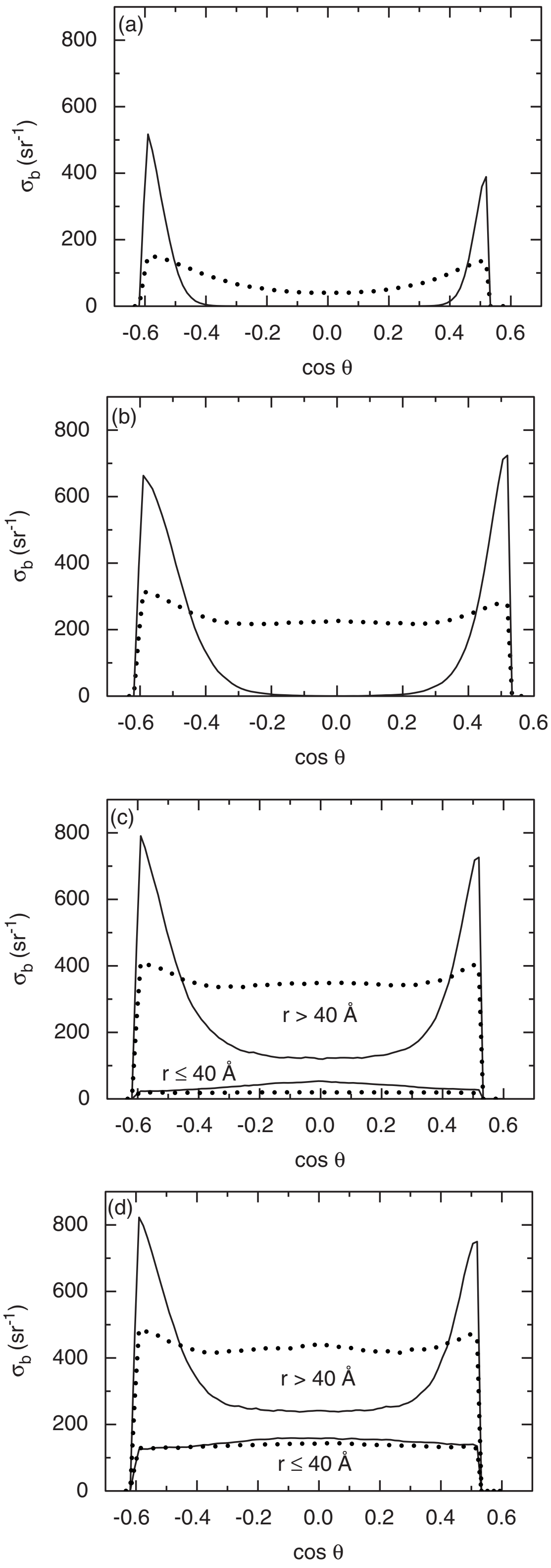

FIG. 4. Bead angular density σ_b along one of the five arclengths connecting a vertex ($\cos\theta=-0.61$) and the midpoint of the opposite edge ($\cos\theta=0.52$) of a pentagon for polyelectrolytes with (a) $N_b=100$, (b) 260, (c) 400, and (d) 600 beads at charge distribution parameter $\lambda=0.1$ (dotted curves) and 1 (solid curves) evaluated separated for the surface layer (40 Å $< r \leq 48$ Å) and the inner region ($r \leq 40$ Å).

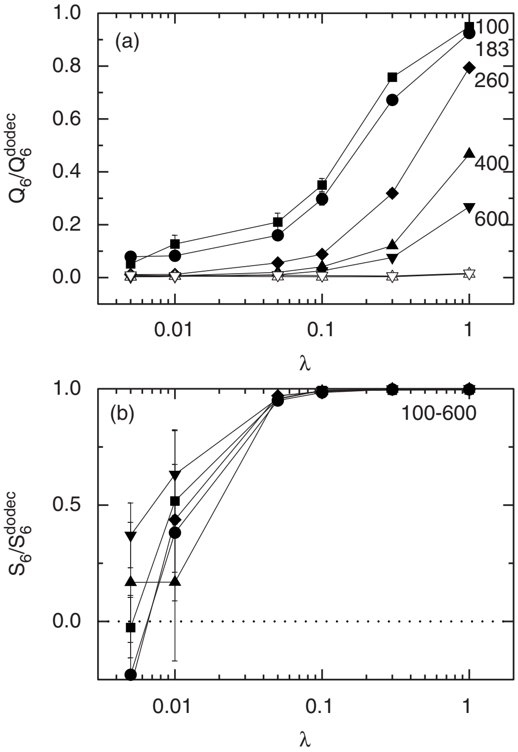

FIG. 5. (a) Normalized order parameter Q_6/Q_6^{dodec} and (b) normalized symmetry parameter S_6/S_6^{dodec} as a function of the charge distribution parameter λ on a semilog scale for encapsidated polyelectrolytes with $N_b=100$, 183, 260, 400, and 600 beads. Q_6/Q_6^{dodec} is given separately for the surface layer (40 Å $< r \leq 48$ Å) (closed symbols) and the inner region ($r \leq 40$ Å) (open symbols), and S_6/S_6^{dodec} is given only for the surface layer.

nificantly between $N_b=260$ and 400, which corresponds to the charge ratio parameter $\beta \approx 1$ and 1.5. Noticeable, at $\lambda=1$ with $N_b=100$ and 183, we have $Q_6/Q_6^{\mathrm{dodec}} \approx 0.95$ implying that nearly all beads are located along the dodecahedral edges (cf. Fig. 3 top right). Hence for a given capsid charge distribution, short chains ($N_b \leq 183$) adhere more easily to the dodecahedral edges formed by the capsid charges than long chains ($N_b \geq 400$) do. This observation will be discussed shortly.

As mentioned earlier, the presence of I_h symmetry of the encapsidated polyelectrolyte can be estimated by the symmetry parameter S_6. Figure 5(b) shows that (i) the data for the normalized symmetry parameter S_6/S_6^{dodec} for beads in the surface layer falls essentially on a master curve, i.e., it is independent of the chain length and (ii) two different regimes are present, viz. $S_6/S_6^{\mathrm{dodec}} \approx 0$ within the uncertainty limits for $\lambda \leq 0.01$, and $S_6/S_6^{\mathrm{dodec}} \approx 1$ for $\lambda \geq 0.05$. Hence the appearance of I_h symmetry occurs at $\lambda \approx 0.05$ and is basically independent of the chain length.

The following picture emerges. At $\lambda \leq 0.01$ the deviation from a constant electrostatic potential generated by the capsid charges inside the capsid deviates too little to establish a polyelectrolyte distribution with a nonspherical symmetry. However I_h symmetry has developed at $\lambda=0.05$, where the electrostatic potential energy difference for a bead being in contact with a vertex and a pentagon center is

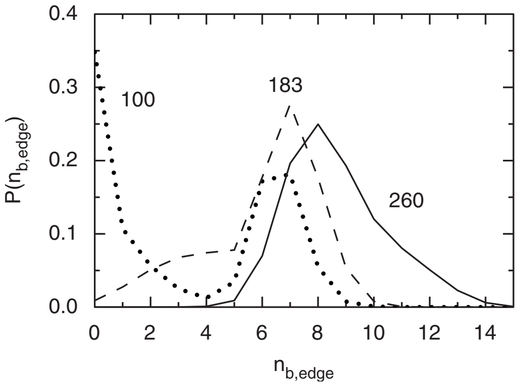

FIG. 6. Probability distribution of the number of beads associated with one edge $P(n_{b,edge})$ for encapsidated polyelectrolytes with the indicated number of beads at charge distribution parameter $\lambda=1$.

$0.3\ kT$. The increased uncertainties of $S_6/S_6^{\rm dodec}$ at the smallest values λ come from the larger lateral fluctuations. Again we emphasize that there is no contradiction of small order parameter $Q_6/Q_6^{\rm dodec}$ and large symmetry parameter $S_6/S_6^{\rm dodec}\approx 1$. The former measure the degree of dodecahedral-like chain structure, while the latter the appearance of I_h symmetry. An I_h symmetry can still appear for weak lateral bead density variation as for $N_b=600$ at $\lambda=0.05$.

We will now, in more detail, examine the path on the dodecahedral graph taken by the polyelectrolyte at $\lambda=1$ and how the path depends on the chain length for $N_b\leq 260$. The basis of our analysis is that the polyelectrolyte chain follows the edges of the dodecahedral formed by the capsid charges as is shown in Figs. 4(a) and 4(b).

Generally, a simple path on a graph, which visits each vertex once, is referred to as a Hamiltonian path. When the path starts and ends at the same vertex, it is referred to as a cycle [6]. A Hamiltonian cycle or a Hamiltonian path cannot cover all edges of a dodecahedral graph; only 20 or 21, respectively, of the 30 edges are visited [6]. Using the assumption that the beads are in contact with the inner capsid surface, we obtain the length of the dodecahedral graph $L^{\rm dodec}\approx 1044$ Å and the length of a Hamiltonian path $L_{\rm H,path}^{\rm dodec}\approx 730$ Å. With the rms bead-bead separation $\langle R_{\rm bb}^2\rangle^{1/2}=5.7$ Å, (i) $N_b=100$ gives the contour length $L=(N_b-1)\times\langle R_{\rm bb}^2\rangle^{1/2}=564\ \text{Å}<L_{\rm H,path}^{\rm dodec}$, (ii) $N_b=183$ gives the contour length $L=1037\ \text{Å}\approx L^{\rm dodec}$, and (iii) $N_b=260$ and $L=1476\ \text{Å}>L^{\rm dodec}$. Moreover, we recall that the polyelectrolyte charge-total capsid charge ratio β is unity at $N_b=260$. The fact that $\beta=1$ is achieved at $L>L^{\rm dodec}$ is related to the longer bead-bead separation as compared to the separation between neighboring capsid charges.

The different paths for different N_b have been characterized by the distribution of the number of beads associated with a dodecahedral edge $n_{b,edge}$. Figure 6 displays the normalized probability distribution $P(n_{b,edge})$ for $N_b=100$, 183, and 260.

Starting with $N_b=100$, we notice that $L\approx 0.5L^{\rm dodec}<L_{\rm H,path}^{\rm dodec}$ and Fig. 6 shows that there are two populations of edges, one population decorated with 6–7 beads and one having 0–2 beads. The reason for not strictly zero beads for the second population is that the chains sometimes make a short loop at the vertices. The probabilities of the two populations are similar, consistent with $L\approx 0.5L^{\rm dodec}$. Hence for the shortest chain, our results show that the chain forms a path covering ≈ 15 of the 30 edges, each of these edges decorated by 6 to 7 beads.

Regarding the chain with $N_b=183$, we have $L\approx L^{\rm dodec}>L_{\rm H,path}^{\rm dodec}$. Figure 6 shows that all edges are decorated with beads, most of them with 6–8 beads but some still only by a few. To resolve the topological impossibility to make a Euler path (a simple path visiting all edges once), the chain forms several short loops each originating from a vertex and follows one dodecahedral edge. These loops extend at most one edge. Sometime these loops are short (2–4 beads), but at other occasions they comprise 8 to 9 beads.

Finally, with $N_b=260$ beads one has $L>L^{\rm dodec}$. At least four beads are associated with one edge, and the probability of finding 10–12 beads between two adjacent vertices increases markedly. Hence longer loops are formed at some of the edges. The electrostatic repulsion within a loop at one dodecahedral edge makes the width of the bead distribution perpendicular to the edge broader [cf. solid curves in panels (a) and (b) of Fig. 4 showing the bead angular density]. The presence of loops implies that the chain makes multiple visits at some of the vertices and enables full coverage of the dodecahedron graph with all beads located in the surface layer.

In our model, at $\lambda=1$ the chain linear charge density is *smaller* than the charge density along the dodecahedron edges, which explain why, after performing a Hamilton path, it is advantageous for the chain to make loops to utilize the otherwise uncovered edges. Moreover, we have considered a flexible chain, where the mean angle formed by three consecutive beads was about 128°, which matches closely the angle made by the dodecahedron edges at the vertex. For stiffer chains, an analysis in terms of Hamilton paths becomes less fruitful due to energetic bending penalties when following the dodecahedral edges close to the vertices.

2. Inner region

The lateral distribution of beads located in the inner region ($r<40$ Å) for polyelectrolytes with $N_b=400$ and 600 beads at various charge distribution parameters are also shown in Figs. 4(c) and 4(d), and the corresponding normalized order $Q_6/Q_6^{\rm dodec}$ parameter is displayed in Fig. 5(a) (open symbols). All representations show that the beads are essentially homogeneously distributed. However, at $\lambda=1$ weak density maxima appear in the center of the pentagons ($\cos\theta=0$). Obviously, the high density of beads in the surface layer along the dodecahedron edges (with a total bead charge exceeding the total capsid charged) slightly affects the lateral location of the beads inside the surface layer through the electrostatic bead-bead repulsion. Here, we obtain the normalized symmetry parameter $S_6/S_6^{\rm dodec}\approx -1.0$, the minus sign demonstrating an accumulation of beads in the inner part of the pentagon.

TABLE II. Average number of capsid counterions $\langle N_{\text{ion}}^{\text{cap}} \rangle$ and polyelectrolyte counterions $\langle N_{\text{ion}}^{\text{pe}} \rangle$ inside the capsid and net charge of the polyelectrolyte-containing capsid $\langle Z_{\text{net}}^{\text{cap}} \rangle$.

N_b	β	λ	$\langle N_{\text{ion}}^{\text{cap}} \rangle$	$\langle N_{\text{ion}}^{\text{pe}} \rangle$	$\langle Z_{\text{net}}^{\text{cap}} \rangle$
100	0.38	0.05	53.3(3)	$<10^{-5}$	106.7(3)
		0.1	53.6(6)	$<10^{-5}$	106.4(6)
		0.3	53.7(3)	$<10^{-5}$	106.3(3)
		1	56.3(3)	$<10^{-5}$	103.7(3)
260	1	0.05	0.010(5)	8.7(5)	8.7(5)
		0.1	0.007(5)	7.7(5)	7.7(5)
		0.3	0.007(3)	6.2(1)	6.2(1)
		1	0.003(1)	3.7(1)	3.7(1)
400	1.54	0.05	$<10^{-5}$	110.0(7)	−30.0(7)
		0.1	<0.007	111.4(6)	−28.6(6)
		0.3	$<10^{-5}$	111.0(5)	−29.0(5)
		1	$<10^{-5}$	113.5(8)	−26.5(8)
600	2.31	0.05	$<10^{-5}$	301.1(8)	−38.9(8)
		0.1	$<10^{-5}$	301.3(7)	−38.7(7)
		0.3	$<10^{-5}$	300.9(8)	−39.1(8)
		1	$<10^{-5}$	303.4(7)	−36.6(7)

C. Small-ion distribution

1. Radial distribution

The number of the small ions inside and outside of the polyelectrolyte-containing capsid has also been determined. Table II gives the average number of capsid counterions $\langle N_{\text{ion}}^{\text{cap}} \rangle$ and the average number of polyelectrolyte counterions $\langle N_{\text{ion}}^{\text{pe}} \rangle$ inside the capsid at a different number of polyelectrolyte beads and different values of the charge distribution parameter. The average net charge of the polyelectrolyte-containing capsid, including the capsid charge and all encapsidated charged species, $\langle Z_{\text{net}}^{\text{cap}} \rangle$, is also given.

First, with the undercharged capsid, i.e., the total capsid charge exceeding the polyelectrolyte charge (β=0.38), there are essentially no polyelectrolyte counterions inside the capsid, and for the overcharged capsid ($\beta>1$) no capsid counterions remain inside the capsid. At both conditions, since $\langle Z_{\text{net}}^{\text{cap}} \rangle \neq 0$, the counterions inside the capsid only partially compensate the net charge of the capsid-polyelectrolyte complex. Second, at the charge-neutral polyelectrolyte-capsid condition (β=1), some polyelectrolyte counterions still appear inside the capsid and are located radially on the inner side of the polyelectrolyte layer, whereas the average number of capsid counterions inside is less than 0.01. The radial separation of the capsid charges located at $r=52$ Å and the polyelectrolyte charges located inside the capsid charges (see Fig. 2) is the origin of this observation [36].

At $\beta\neq 1$, an increased charge distribution parameter λ leads to an increased number of counterions, making $\langle Z_{\text{net}}^{\text{cap}} \rangle$ smaller in magnitude. At β=1, the number of polyelectrolyte counterions reduces more than 50% as λ is increased from 0–1. This reduction is a consequence of the smaller capsid-charge–polyelectrolyte-charge separation occurring at λ=1 [Fig. 2(b)].

2. Lateral distribution inside the capsid

The lateral distribution of the small ions has been analyzed in the same way as the lateral distribution of the polyelectrolyte beads. Generally, the small ions were also accumulated at or near the inner capsid surface but their distributions were less askew as compared to the polyelectrolyte beads and no well-defined surface layer could be assigned. Therefore all small ions inside the capsid are included in the lateral distribution analysis, keeping in mind that a lateral heterogeneous distribution is largest near the inner capsid surface.

Figure 7 shows angular density of the small ions σ_{ion} along the arclength from a vertex to the midpoint of the opposite edge of a pentagon (in the same way as for the bead density shown in Fig. 4) for chains with N_b=100, 260, and 600 beads at various values of the charge distribution parameter. For the undercharged capsid with N_b=100, only capsid counterions reside inside the capsid and these counterions display an increased lateral ordering at increasing λ [Fig. 7(a)], in a similar manner as the polyelectrolyte beads do [Fig. 4(a)]. However, the degree of ordering is reduced as compared to the order of the beads. Since the capsid is undercharged, it is reasonable that the capsid counterions display a similar pattern as the polyelectrolyte beads do. Regarding the charge-neutral polyelectrolyte-capsid complex obtained with N_b=260, the polyelectrolyte counterions are essentially laterally homogeneously distributed at small λ, but display a significant heterogeneous distribution at λ=1. As mentioned earlier, a substantial fraction of these counterions form a layer on the inner side of the polyelectrolyte layer, and the increased lateral counterion heterogeneity reflects the increased heterogeneous polyelectrolyte bead distribution. Finally, with an overcharged capsid obtained with N_b=600, polyelectrolyte counterions are laterally homogeneously distributed inside the capsid even at λ=1. About 2/3 of the counterions reside in the inner polyelectrolyte region where the beads are laterally homogeneously distributed [Fig. 4(d)].

D. Comparison with experiments

Experimental studies on viral RNA packaging have shown that the viral RNA genome adjacently located to the capsid proteins for several T=1 and 3 viruses display a dodecahedral structure [7,8,17,42]. Different arrangements of RNA are possible with the double-stranded secondary structure constituting the edges of the dodecahedron. The chain configuration at the vertices could not be visualized, but the presence of unpaired "bubbles" at the vertices, possessing larger flexibility than the double-stranded RNA backbone, is inferred [6]. Some studies suggested that the sequence and the length of the viral RNA genome are not important for reaching the dodecahedral structure, the flexibility of RNA being exploited to force the RNA into a shape of a dodecahedon [7,42]. Inspection of the base-pairing arrangements in various RNA genomes suggested that the presence of individual secondary structural elements joined by single-stranded intervals is likely specific for a dodecahedrally packed RNA genome [43].

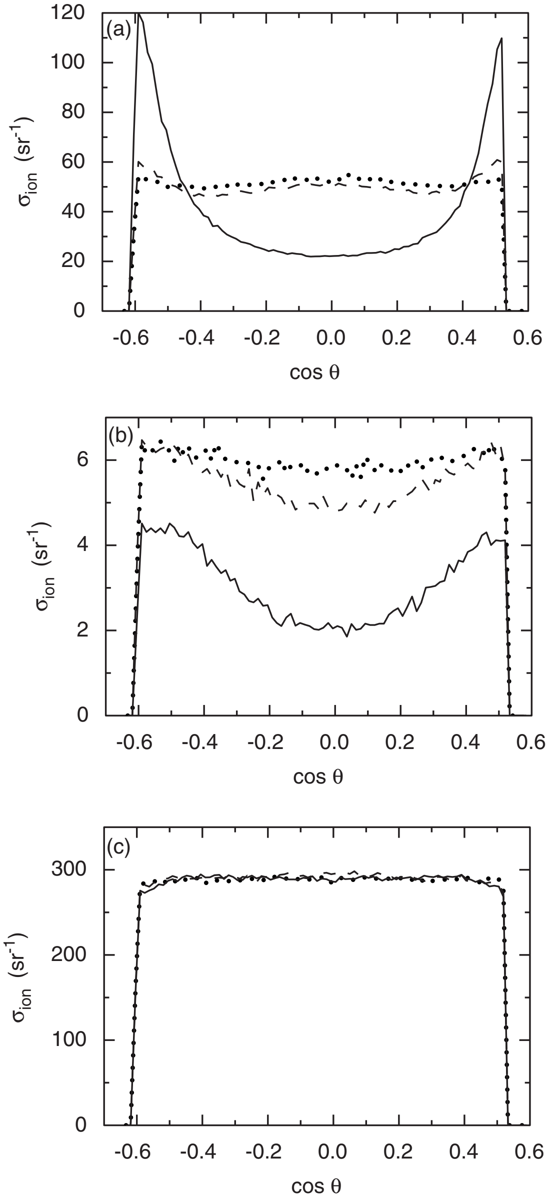

FIG. 7. Angular density σ_{ion} of small ions located inside the capsid and along one of the five arc lengths connecting a vertex ($\cos\theta=-0.61$) and the midpoint of the opposite edge ($\cos\theta=0.52$) of a pentagon. (a) Capsid counterion for $N_b=100$, (b) polyelectrolyte counterion for $N_b=260$, and (c) polyelectrolyte counterion for $N_b=600$ at charge distribution parameter $\lambda=0.1$ (dotted curves), 0.3 (dashed curves), and 1 (solid curves).

In the present study, we follow the coarse-grained approach, in which the RNA sequence is replaced by a chain of identical beads. Our focus concerns the effect of a dodecahedral capsid charge distribution on the genome packaging at increasing lateral heterogeneity. In particular, the electrostatic potential generated by the capsid charges of the pariacoto virus is closely reproduced by our model system at $\lambda \approx 0.4$ (Fig. 1). Though the genome was treated as a homopolymeric chain, our model predictions are in line with the experimental findings that the genome near the inner capsid surface also display a dodecahedral arrangement [8]. Hence our findings support that genome-capsid electrostatic interactions play an important role for the lateral organization and for the path adopted by the genome in the dodecahedral graph. After this establishment, more refined approaches should be employed, in particular, to examine the role of the secondary RNA structure for the genome arrangement near the capsid surface.

IV. SUMMARY

Inspired by recent experimental observations that the genome in some viruses possesses a dodecahedral structure inside the icosahedrally shaped capsid, presumably driven by electrostatic interactions, we have constructed a coarse-grained model to examine the propensity of a flexible polyelectrolyte to attain a dodecahedral structure. Our model includes electrostatic interactions, excluded volume interactions, and bond and bending potentials to establish a polyelectrolyte with a given flexibility, here the bare persistence length was smaller than the capsid radius as for the case for *ss*RNA containing viruses.

On the basis of our minimalistic viral model, the structure of the encapsidated polyelectrolyte and the distribution of small ions have been examined for different polyelectrolyte lengths at constant linear charge density and various distributions of capsid charges at constant total capsid charge. The distribution of the capsid charges ranged from a homogeneous distribution to a distribution where all capsid charges were positioned on the edges of a dodecahedon, as the charge distribution parameter λ was varied from 0 to 1. Our main findings and conclusions are as follows.

(a) The radial distribution of the polyelectrolyte beads and the partitioning of small ions between the interior and the exterior of the capsid were only weakly dependent on the charge distribution parameter. Beads were accommodated in two distinct radial regions, a surface layer and an inner region. At increased capsid charge heterogeneity, the polyelectrolyte became stronger adsorbed to the inner capsid surface and the absolute value of the net charge of the capsid, including the charged species inside the capsid, became smaller.

(b) The lateral distribution of the polyelectrolyte beads was strongly affected by the capsid charge distribution. At large λ, the polyelectrolyte in the layer closest to the inner capsid surface also displayed a dodecahedral structure owing to its attractive Coulomb interaction with the capsid charges. The shortest polyelectrolyte was the most affected. Independently of the chain length, $\lambda=0.05$ was sufficient to produce I_h symmetry of the encapsidated polyelectrolyte. In those cases where the polyelectrolyte charge exceeded the capsid charge, a part of the polyelectrolyte homogeneously populated the inner region.

(c) At $\lambda=1$, polyelectrolyte beads were strongly located along the dodecahedral graph and the concept of the Hamiltonian path could be applied to examine the chain conformation. Chains shorter than the Hamiltonian path made a simple path along the edges of the dodecahedron, whereas longer chains passed most of the vertices once but some of the vertices twice in opposite directions with an intermediate loop along an edge.

(d) Dodecahedral structure was in most cases also found for encapsidated counterions at large λ unless the polyelectrolyte-capsid complex is overcharged ($N_b > 260$). At $\beta < 1$, capsid counterions were preferentially positioned on the polyelectrolyte-free vertices, whereas at $\beta = 1$, some polyelectrolyte counterions are found near the polyelectrolyte surface layer.

Despite that our minimalistic model (i) leaves out essentially all molecular details, such as the capsid structure and its more elaborated charge distribution, including basic peptide tails [44], (ii) neglects that the secondary structure of viral *ss*RNA is a branched polymer [6] rather than a linear one, and (iii) does not contain any added salt as compared to physiological conditions, hence the electrostatic interactions are here less screened, we believe that simple models as the present one constitute important initial steps to establish the connection between interactions in viral systems and their structures. In the present case, we have established a model where (i) the polyelectrolyte close to the inner capsid surface adopts a dodecahedral structure inherited from the capsid charge distribution and (ii) the polyelectrolyte in the inner region of the capsid displays a laterally homogeneous distribution; two features reported for $T = 3$ viruses.

ACKNOWLEDGMENTS

We are gratefully indebted to Professor Robijn Bruisma for fruitful discussions at early stages of this work and for initiating the study of the symmetry of encapsidated RNA. Financial support from the Swedish Research Council (V.R.) is gratefully acknowledged.

[1] P. K. Purohit, M. M. Inamdar, P. D. Grayson, T. M. Squires, and J. Kondev, Biophys. J. **88**, 851 (2005).

[2] J. Lepault, J. Dubochet, W. Baschong, and E. Kellenberger, EMBO J. **6**, 1507 (1987).

[3] M. E. Cerritelli, N. Cheng, A. H. Rosenberg, C. E. McPherson, F. P. Booy, and A. C. Steven, Cell **91**, 271 (1997).

[4] A. Fokine, P. R. Chipman, P. G. Leiman, V. V. Mesyanzhinov, V. B. Rao, and M. G. Rossmann, Proc. Natl. Acad. Sci. U.S.A. **101**, 6003 (2004).

[5] R. F. Bruinsma, Eur. Phys. J. E **19**, 303 (2006).

[6] J. Rudnick and R. Bruinsma, Phys. Rev. Lett. **94**, 038101 (2005).

[7] K. N. Johnson, L. Tang, J. E. Johnson, and L. A. Ball, J. Virol. **78**, 11371 (2004).

[8] L. Tang, K. N. Johnson, L. A. Ball, T. Lin, M. Yeager, and J. E. Johnson, Nat. Struct. Biol. **8**, 77 (2001).

[9] G. A. Bentley, A. Lewit-Bentley, L. Liljas, U. Skoglund, M. Roth, and T. Unge, J. Mol. Biol. **194**, 129 (1987).

[10] S. B. Larson, S. Koszelak, J. Day, A. Greenwood, J. A. Doods, and A. McPherson, J. Mol. Biol. **231**, 375 (1993).

[11] S. B. Larson, J. Day, A. Greenwood, and A. McPherson, J. Mol. Biol. **277**, 37 (1998).

[12] B. Bottcher and R. A. Crowther, Structure (London) **4**, 387 (1996).

[13] A. V. Fisher and J. E. Johnson, Nature (London) **361**, 176 (1993).

[14] J. P. Wery, V. S. Reddy, M. V. Hosur, and J. E. Johnson, J. Mol. Biol. **235**, 565 (1994).

[15] P. Gouet, J. M. Diprose, J. M. Grimes, R. Malby, J. N. Burroughs, and S. Zientara, Cell **97**, 481 (1999).

[16] R. Koning, S. V. Worm, J. R. Plaisier, J. V. Duin, J. P. Abrahams, and H. Koerten, J. Mol. Biol. **332**, 415 (2001).

[17] H. H. Bink and C. W. Pleij, Arch. Virol. **147**, 2261 (2002).

[18] J. A. Speir, S. M. Munshi, G. Wang, T. S. Baker, and J. E. Johnson, Structure (London) **3**, 63 (1995).

[19] D. Zhang, R. Konecny, N. A. Baker, and J. A. McCammon, Biopolymers **75**, 323 (2004).

[20] R. A. Mastico, S. J. Talbot, and P. G. Stockley, J. Gen. Virol. **74**, 541 (1993).

[21] L. W. Enquist, R. M. Krug, V. R. Racaniello, A. M. Skalka, S. J. Flint, and S. J. Flint, *Principles of Virology: Molecular Biology, Pathogenesis, and Control* (ASM Press, Washington, 2000).

[22] G. Corongiu and E. Clementi, Biopolymers **20**, 551 (1981).

[23] G. L. Seibel, U. C. Singh, and P. A. Killman, Proc. Natl. Acad. Sci. U.S.A. **82**, 6537 (1985).

[24] L. E. Guldbrand, T. R. Forrester, and R. M. Lynden-Bell, Mol. Phys. **67**, 473 (1989).

[25] A. Laaksonen, Chem. Phys. **129**, 175 (1989).

[26] T. R. Forrester and I. R. McDonald, Mol. Phys. **72**, 643 (1991).

[27] P. Smith, R. M. Lynden-Bell, and W. Smith, Phys. Chem. Chem. Phys. **2**, 1305 (2000).

[28] D. L. Beveridge and K. J. McConnell, Curr. Opin. Struct. Biol. **10**, 182 (2000).

[29] H. Schiessel, W. M. Gelbart, and R. Bruinsma, Biophys. J. **80**, 1940 (2001).

[30] H. Schiessel, J. Widom, R. F. Bruinsma, and W. M. Gelbart, Phys. Rev. Lett. **86**, 4414 (2001).

[31] K.-K. Kunze and R. R. Netz, Phys. Rev. E **66**, 011918 (2002).

[32] T. Sakaue, K. Yoshikawa, S. H. Yoshimura, and K. Takeyasu, Phys. Rev. Lett. **87**, 078105 (2001).

[33] C. Holm, P. Kekicheff, and R. Podgornik, *Electrostatics Effects in Soft Matter and Biophysics* (Kluwer Academic, Dodrecht, 2001).

[34] P. Linse, Adv. Polym. Sci. **185**, 111 (2005).

[35] P. Linse and V. Lobaskin, J. Chem. Phys. **112**, 3917 (2000).

[36] D. G. Angelescu, R. Bruinsma, and P. Linse, Phys. Rev. E **73**, 041921 (2006).

[37] P. L. Freddolino, A. S. Arkhipov, S. B. Larson, A. McPherson, and K. Schulten, Structure (London) **14**, 437 (2006).

[38] A. Akinchina and P. Linse, Macromolecules **35**, 5183 (2002).

[39] P. Linse, MOLSIM, Version 4.0, Lund University, Sweden (2005).

[40] P. J. Steinhardt, D. R. Nelson, and M. Ronchetti, Phys. Rev. B **28**, 784 (1983).

[41] D. M. Brink and G. R. Satchler, *Angular Momentum* (Claredom Press, Oxford, 1979).

[42] M. Tihova, K. A. Dryden, T. L. Le, S. C. Harvey, J. E. Johnson, M. Yeager, and A. Schneemann, J. Virol. **78**, 2897 (2004).
[43] Y. G. Kuznetsov, S. Daijogo, J. Zhou, B. L. Semler, and A. McPherson, J. Mol. Biol. **347**, 41 (2005).
[44] V. A. Belyi and M. Muthukumar, Proc. Natl. Acad. Sci. U.S.A. **103**, 17174 (2006).
[45] http://viperdb.scripps.edu/